Theory of the electric field controlled antiferromagnetic spin Hall oscillator and detector

G. Consolo, G. Valenti, A. R. Safin, S. A. Nikitov, V. Tyberkevich, and A. Slavin

Theory of Electric-Field-Controlled Antiferromagnetic Spin-Hall Oscillator and Detector

G. Consolo[1], G. Valenti[2], A.R. Safin[3,4], S.A. Nikitov[3,5], V. Tyberkevich[6], A. Slavin[6]

[1]*Department of Mathematical, Computer, Physical and Earth Sciences, University of Messina, 98166 Messina, Italy*

[2]*Department of Engineering, University of Messina, 98166 Messina, Italy*

[3]*Kotel'nikov Institute of Radioengineering and Electronics, Russian Academy of Sciences, 125009 Moscow, Russia*

[4]*National Research University "Moscow Power Engineering Institute", 111250 Moscow, Russia*

[5]*Moscow Institute of Physics and Technology, Dolgoprudny 141701, Moscow Region, Russia*

[6]*Oakland University, Department of Physics, Rochester, Michigan, 48309, USA*

Abstract

A theory of electrically-controlled THz-frequency auto-oscillator, based on a tri-layer hetero-structure comprised of a piezoelectric (PZ) ceramics, an NiO-based antiferromagnet (AFM), and a heavy metal (HM), is developed in the framework of the well-established AFM sigma-model. It is assumed that the magnetostrictive AFM is monocrystalline and monodomain, and has mixed biaxial and cubic anisotropy. The frequency of the antiferromagnetic resonance (AFMR) of the hetero-structure in a passive subcritical regime is calculated as a function of the following parameters: the choice of the ceramic PZ material and of its poling direction, modulus and orientation of the static electric field applied to the PZ layer, and the magnitude of the driving electric current injected into the HM layer. It is shown that the AFMR frequency of the hetero-structure, and the threshold value of the driving current for THz-frequency generation, depend on the total AFM anisotropy, which can be substantially reduced by the bias electric field in the case when this field is collinear to the PZ poling direction. It is also shown that the variation of the PZ poling direction in respect to the bias electric field provides an additional degree of freedom that can be used to optimize the performance of AFM-based generators and detectors of THz-frequency signals.

1.   Introduction

Recently, antiferromagnetic (AFM) materials have attracted a lot of attention of researchers due to the possibility of development of AFM-based magnetic-bias-free THz-frequency signal processing devices [1]. AFM do not produce stray dipolar magnetic fields, and, therefore, are not sensitive to the perturbation created by the external magnetic fields. They demonstrate ultrafast spin dynamics at THz frequencies [2] due to the presence in AFM of very strong internal magnetic fields of the exchange nature, that keep the AFM sub-lattices antiparallel to each other. These properties of AFMs make them appealing for

applications in magnetic memory devices [3], electrically tunable oscillators [4, 5] and detectors [6-8]. However, for applications, it is necessary to find effective means of external control of magnetization states of AFMs, since magnetic fields used to control ferromagnets are not effective with AFMs.

Previously [9], it was shown theoretically that in a heterostructure comprising piezoelectric, dielectric antiferromagnetic crystal, and heavy metal (PZ/AFM/HM), it is possible to control the biaxial anisotropy of the AFM layer by applying a dc voltage across the PZ layer. It was shown that the variation of the dc voltage across the PZ layer and/or the variation of the dc electric current in the HM layer allows one to control the antiferromagnetic resonance (AFMR) frequency of the AFM in a passive (subcritical) regime, and, also, to reduce the threshold driving current of the current-induced terahertz-frequency oscillations. The voltage-induced reduction of the oscillation threshold leads to the proportional reduction of the amplitude of the terahertz-frequency signal generated in the active (supercritical) regime. These results were obtained under the simplifying assumption that the studied AFM is NiO-like, and has a simple bi-axial anisotropy, and that the poling direction of the PZ material and the externally applied bias electric field are parallel to each other.

In our current work, we present a *generalized* theory of the electric-field control of the AFM properties, taking into account both *biaxial* and *cubic* anisotropy of the AFM and varying dc voltage across the PZ layer and the dc electric current in the HM. We focus on the characterization of the AFMR frequency excited in the passive subcritical regime as a function of different features, specifically: choice of the ceramic PZ material and of its poling direction Π, modulus and orientation of the electric field $\mathbf{E}$ induced by a dc voltage applied to the PZ, that is employed to generate and transfer strains on the AFM layer, influence of the electric current injected into the HM, crystal symmetry of the AFM layer and magnetoelastic field, arising from the mechanical coupling between AFM and PZ. The account for the mixed biaxial and cubic anisotropy is an attempt to reproduce more closely the complex crystal symmetry of AFM materials like NiO. At the same time, the possibility to vary the PZ poling direction provides an additional degree of freedom that is here used to optimize the performance of AFM-based generators or/and detectors of THz-frequency signals.

The paper is organized as follows. In Sec.1, an introduction to voltage- (or electric-field-) controlled AFM spintronics is presented. In Sec.2, we consider a mathematical model of the PZ/AFM/Pt heterostructure with a longitudinal electric field applied to it. We derive a general linear tensorial relation between the vector of the applied electric field and the electric-field-induced change in the AFM anisotropy tensor with both biaxial and cubic anisotropies. In Sec. 2.1, we solve the static equation of the "sigma-model" [10,11] to determine the ground state of the Neel vector. In Sec.2.2, we consider the small

perturbations near the equilibrium state by solving the dynamic equation, and find the eigenfrequencies of the system as functions of the external electric field applied to PZ and density of the dc electric current in HM. In Sec.3 we present the results of numerical study based on the theoretical results obtained earlier. We consider two cases, where dielectric polarization is parallel and perpendicular to the electric field. Discussion and conclusions of the obtained results are presented in Sec. 4.

2. Electric-field-controlled auto-oscillation dynamics in a trilayer piezoelectric/antiferromagnet/heavy-metal heterostructure

Let us consider a trilayer piezoelectric (PZ)/antiferromagnet (AFM)/heavy-metal (HM) heterostructure presented in Fig.1. The very thin HM layer is traversed by an electric current J that, due to spin-Hall effect, becomes spin-polarized, and creates a perpendicular spin-current $\mathbf{p}$ that, in turn, exerts a spin-transfer-torque on the AFM sublattice magnetizations, $\mathbf{m}^{(1)}$ and $\mathbf{m}^{(2)}$. At the same time, the AFM layer is also tightly coupled to a layer of a piezoelectric material which experiences a mechanical deformation upon the application of a bias voltage via lateral electrodes. The thick PZ layer transfers the voltage-induced mechanical strain to the thin AFM through a common interface. Therefore, the AFM is simultaneously subject to the effects arising from the current-induced spin-transfer torque and voltage-induced mechanical strain.
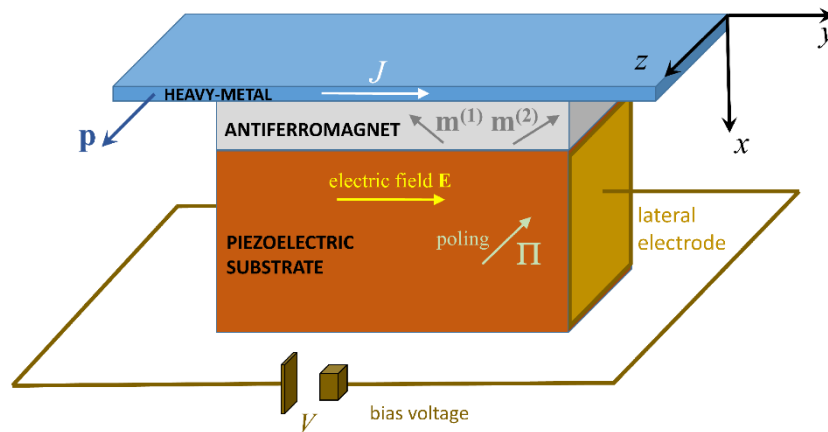
Figure 1. Schematics of the tri-layer PZ/AFM/HM structure
(the directions of the vector quantities, and of the position of the lateral electrodes, are shown here as an example, and can be varied).

Magnetization dynamics in the AFM is ruled by a pair of Landau-Lifshitz-Gilbert-Slonczewski (LLGS) equations written for AFM sublattice magnetizations:

$$\frac{d\mathbf{m}^{(\xi)}}{dt} = \gamma\left(\mathbf{h}_{EFF}^{(\xi)} \times \mathbf{m}^{(\xi)}\right) + \alpha_G\left(\mathbf{m}^{(\xi)} \times \frac{d\mathbf{m}^{(\xi)}}{dt}\right) + \tau\left(\mathbf{m}^{(\xi)} \times \left(\mathbf{m}^{(\xi)} \times \mathbf{p}\right)\right) \qquad (\xi = 1, 2) \qquad (1)$$

where $\mathbf{m}^{(\xi)} = \mathbf{M}^{(\xi)}/M_S$ represents the normalized magnetization of the ξ-th sublattice, where M_S is the saturation magnetization, γ is the gyromagnetic ratio, α_G is the Gilbert damping, $\tau = \sigma J$ is the spin-transfer-torque strength proportional to the current density J (M_S, α_G and σ are assumed to be the same for both sublattices), $\mathbf{h}_{EFF}^{(\xi)}$ is the normalized effective magnetic field acting on the ξ-th sublattice, the "over dot" notation stands for partial time derivative, and the symbol "$\times$" denotes the vector product.

In the absence of external bias magnetic fields, we assume that the effective magnetic field in AFM is the sum of the fields produced by the exchange interaction, magnetocrystalline anisotropy and magnetoelastic interaction:

$$\mathbf{h}_{EFF}^{(\xi)} = \mathbf{h}_{EXC}^{(\xi)} + \mathbf{h}_{ANI}^{(\xi)} + \mathbf{h}_{MEL}^{(\xi)} \qquad (\xi = 1, 2) \qquad (2)$$

Expressing all the quantities in SI units, we get the following expression for the exchange fields:

$$\mathbf{h}_{EXC}^{(\xi)} = -\frac{H_{exc}}{2M_S}\Xi\,\mathbf{m}^{(\xi)}, \qquad \Xi = \begin{bmatrix} 0 & 1 \\ 1 & 0 \end{bmatrix} \qquad (3)$$

Here the minus sign reflects the fact that the exchange field acting on the first (second) sublattice directs its magnetization oppositely to the second (first) one, thus enforcing the antiferromagnetic order. It is also worth mentioning, that the exchange field H_{exc} is much larger than any other field acting in the AFM.

In contrast with [4,9], we consider here a more general expression for the magnetocrystalline anisotropy field to describe realistic AFM materials exhibiting rather complex anisotropy patterns with competing cubic and uniaxial (or biaxial) anisotropies [10-17]. This is, for instance, the case for such commonly used antiferromagnetic material, as the NiO, which is a *cubic* crystal, which also exhibits an easy-plane anisotropy with the easy-axial anisotropy in the easy plane.

We take into account all these anisotropy contributions as follows:

$$\mathbf{h}_{ANI}^{(\xi)} = \mathbf{h}_{BIAX}^{(\xi)} + \mathbf{h}_{CUB}^{(\xi)} \qquad (\xi = 1, 2), \qquad (4a)$$

$$\mathbf{h}_{BIAX}^{(\xi)} = -\frac{2K_H}{\mu_0 M_S^2}\left(\mathbf{e_z} \cdot \mathbf{m}^{(\xi)}\right)\mathbf{e_z} + \frac{2K_E}{\mu_0 M_S^2}\left(\mathbf{e_y} \cdot \mathbf{m}^{(\xi)}\right)\mathbf{e_y}, \qquad (4b)$$

$$\mathbf{h}_{CUB}^{(\xi)} = -\frac{2K_C}{\mu_0 M_S^2}\left(m_x^{(\xi)}\left(1 - m_x^{(\xi)2}\right)\mathbf{e_x} + m_y^{(\xi)}\left(1 - m_y^{(\xi)2}\right)\mathbf{e_y} + m_z^{(\xi)}\left(1 - m_z^{(\xi)2}\right)\mathbf{e_z}\right), \qquad (4c)$$

where $\mathbf{e_z}$ and $\mathbf{e_y}$ denote the hard and the easy axis, respectively. Note, that thanks to the normalization constraint $m_x^{(\xi)2} + m_y^{(\xi)2} + m_z^{(\xi)2} = 1$, the easy-axis contribution along $\mathbf{e_x}$ may be enclosed into the previous

ones. In the equations (4b, c) μ_0 is the vacuum permeability, whereas K_H, K_E and K_C are the hard, uniaxial and cubic anisotropy constants, respectively.

The magnetoelastic field can be expressed as a partial derivative of the magnetoelastic energy W_{MEL} with respect to the magnetization [18-23]:

$$\mathbf{h}_{MEL}^{(\xi)} = -\frac{1}{\mu_0 M_S^2} \frac{\partial W_{MEL}^{(\xi)}}{\partial \mathbf{m}^{(\xi)}} \qquad (\xi = 1, 2) \tag{5a}$$

and, for a cubic material, W_{MEL} has the form:

$$W_{MEL}^{(\xi)} = B_1 \left(\varepsilon_{xx} m_x^{(\xi)^2} + \varepsilon_{yy} m_y^{(\xi)^2} + \varepsilon_{zz} m_z^{(\xi)^2} \right) + 2B_2 \left(\varepsilon_{xy} m_x^{(\xi)} m_y^{(\xi)} + \varepsilon_{xz} m_x^{(\xi)} m_z^{(\xi)} + \varepsilon_{yz} m_y^{(\xi)} m_z^{(\xi)} \right) + c.c. \tag{5b}$$

where "*c.c.*" stands for the "terms independent of magnetization", while the magnetoelastic coefficients, B_1 and B_2, combine the two magnetostrictive coefficients (λ_{100} and λ_{111}), and the three elastic constants (c_{11}, c_{12} and c_{44}) as follows:

$$B_1 = -\frac{3}{2} \lambda_{100} (c_{11} - c_{12})$$
$$B_2 = -3\lambda_{111} c_{44} \tag{6}$$

Let us also remember, that for materials belonging to the cubic crystal classes $\bar{4}3m, 432$ and $m\bar{3}m$, that, typically, undergo *isochoric* magnetostrictive deformations, the fourth-order elasticity tensor ⬜ is expressed as (in Voigt notation):

$$⬜ = \begin{bmatrix} c_{11} & c_{12} & c_{12} & & & \\ c_{12} & c_{11} & c_{12} & & [\mathbf{0}] & \\ c_{12} & c_{12} & c_{11} & & & \\ & & & c_{44} & 0 & 0 \\ & [\mathbf{0}] & & 0 & c_{44} & 0 \\ & & & 0 & 0 & c_{44} \end{bmatrix}. \tag{7}$$

Note that, for isotropic materials, the number of the above introduced independent constants is reduced, because in that case $\lambda_{100} = \lambda_{111} = \lambda_S$ and $c_{44} = (c_{11} - c_{12})/2$, so that $B_1 \equiv B_2$. These latter assumptions were used in some previous works dealing with NiO [9, 24].

In (5b), the quantities $\varepsilon_{xx}, \varepsilon_{yy}, \varepsilon_{zz}$ measure the mechanical strains along the principal axes of the AFM whereas $\varepsilon_{xy}, \varepsilon_{xz}, \varepsilon_{yz}$ denote the shear strains. All these strains originate from the application of a fixed bias electric voltage V to the PZ via two lateral electrodes. Such electrodes generate, in turn, an electric field $\mathbf{E}$ that induces an elongation (contraction) of the PZ width along the direction of the electric field, together with a contraction (elongation) in the two orthogonal directions. In our analysis, we don't fix *a priori* the

relative orientation of the PZ polarization **Π** and applied electric field **E,** since it constitutes a degree of freedom which we shall use to optimize the key parameters associated with the auto-oscillations of the studied structure.

Let us assume that, since the AFM layer is substantially thinner than the PZ layer, the strain variations along the AFM film thickness (*x* axis) can be disregarded. Moreover, the total strains acting on each sublattice of the AFM layer are assumed to be constant in time and uniform in space. Therefore, to identify the above mentioned strain components, we shall apply mechanical boundary conditions at both the top and bottom *yz* surfaces of the AFM layer.

In such an identification procedure, let us consider that, in the layered structures similar to the one shown in Fig.1, typically, a thin layer of an AFM crystal is grown on a relatively thick piezoelectric substrate and, then, a very thin layer of a HM is sputtered on top of the AFM layer. In such a case, it is reasonable to assume that the thin layers of the AFM and HM will not affect the mechanical properties of the piezoelectric, while the ultra-thin HM layer will not strongly influence the mechanical properties of the AFM.

Therefore, at the *bottom yz* surface, we assume that an ideal acoustic contact between PZ and AFM is realized, so that the planar strains $\varepsilon_{yy}, \varepsilon_{yz}, \varepsilon_{zz}$ are imposed by the PZ layer and fully transferred to the AFM [9,23,25]:

$$P_{ik}\varepsilon^{PZ}_{kl}P_{lj} = P_{ik}\varepsilon_{kl}P_{lj} = \varepsilon^{IF}_{ij} \quad \Rightarrow \quad \begin{cases} \varepsilon^{PZ}_{yy} = \varepsilon_{yy} = \varepsilon^{IF}_{yy} \\ \varepsilon^{PZ}_{yz} = \varepsilon_{yz} = \varepsilon^{IF}_{yz} \\ \varepsilon^{PZ}_{zz} = \varepsilon_{zz} = \varepsilon^{IF}_{zz} \end{cases} \tag{8}$$

where $P_{ij} = I_{ij} - n_i n_j$ is the projector on the AFM/PZ interface, I_{ij} is the identity matrix and n_i the unit vector orthogonal to the AFM/PZ interface, and the Einstein summation convention is here used.

Let **d** be the third-order strain-piezoelectric tensor that allows to relate the electric field **E**=(E_x, E_y, E_z) generated by the application of a dc bias voltage *V* across the lateral electrodes to the strains ε^{PZ}_{kl} generated in the PZ layer as:

$$\varepsilon^{PZ}_{kl} = d_{ijk}E_k \tag{9}$$

The structure of the tensor **d** depends on the direction of the dielectric polarization, as well as on the crystal symmetry of the PZ material. For simplicity, let us restrict our analysis to a PZ layer made from a polarized ceramics that is known to be transversely isotropic. In this case, the tensor **d** is expressed in terms of three independent coefficients (d_1, d_2, d_4). Moreover, let **Π**, a constant unit vector, represent the direction of the

axis of rotational symmetry (or the poling direction) of the PZ ceramics. Assuming the vector $\mathbf{\Pi}$ to be directed along one of the reference axes, the tensor $\mathbf{d}$ takes the following forms (in Voigt notation) [26]:

$$\mathbf{d}(\mathbf{\Pi} \equiv \mathbf{e_x}) = \begin{bmatrix} d_1 & 0 & 0 \\ d_2 & 0 & 0 \\ d_2 & 0 & 0 \\ 0 & 0 & 0 \\ 0 & 0 & d_4 \\ 0 & d_4 & 0 \end{bmatrix}; \quad \mathbf{d}(\mathbf{\Pi} \equiv \mathbf{e_y}) = \begin{bmatrix} 0 & d_2 & 0 \\ 0 & d_1 & 0 \\ 0 & d_2 & 0 \\ 0 & 0 & d_4 \\ 0 & 0 & 0 \\ d_4 & 0 & 0 \end{bmatrix}; \quad \mathbf{d}(\mathbf{\Pi} \equiv \mathbf{e_z}) = \begin{bmatrix} 0 & 0 & d_2 \\ 0 & 0 & d_2 \\ 0 & 0 & d_1 \\ 0 & d_4 & 0 \\ d_4 & 0 & 0 \\ 0 & 0 & 0 \end{bmatrix} \quad (10)$$

At the *top yz* surface the AFM layer, by assuming that the very thin heavy metal layer takes a negligible role in the mechanical response of the AFM, this interface is treated as if it were free. The application of traction boundary conditions at this surface results in vanishing of the normal components of the Cauchy stress tensor σ_{ij} [9, 25]:

$$\sigma_{ij} n_j = \square_{ijkl} \varepsilon_{kl} n_j = \mathbf{0}, \quad \text{with } \mathbf{n} = \mathbf{e_x} \quad \Rightarrow \quad \begin{cases} \varepsilon_{xx} = -\eta \left(\varepsilon_{yy} + \varepsilon_{zz} \right) \\ \varepsilon_{xy} = \varepsilon_{xz} = 0 \end{cases} \quad (11)$$

where $\eta = c_{12}/c_{11}$. In (11) we assumed a linear constitutive relation between the stress and strain, and, also, neglected the magnetostriction strain tensor.

Combining (7) - (11), we get the expressions for the strain tensor acting on the AFM for three different poling directions of the PZ $\mathbf{\Pi}$ as a function of the components of the electric field $\mathbf{E}$:

$$\varepsilon(\mathbf{\Pi} \equiv \mathbf{e_x}) = \begin{bmatrix} -2\eta & 0 & 0 \\ 0 & 1 & 0 \\ 0 & 0 & 1 \end{bmatrix} d_2 E_x \quad (12a)$$

$$\varepsilon(\mathbf{\Pi} \equiv \mathbf{e_y}) = \begin{bmatrix} -\eta(d_1 + d_2) E_y & 0 & 0 \\ 0 & d_1 E_y & d_4 E_z \\ 0 & d_4 E_z & d_2 E_y \end{bmatrix} \quad (12b)$$

$$\varepsilon(\mathbf{\Pi} \equiv \mathbf{e_z}) = \begin{bmatrix} -\eta(d_1 + d_2) E_z & 0 & 0 \\ 0 & d_2 E_z & d_4 E_y \\ 0 & d_4 E_y & d_1 E_z \end{bmatrix} \quad (12c)$$

In (5b) and (11), we disregarded the contribution arising from the magnetostriction. The reason is that the magnetostriction energy

$$W_{MS}^{(\xi)} = K_{MS}\left(m_x^{(\xi)2}m_y^{(\xi)2} + m_x^{(\xi)2}m_z^{(\xi)2} + m_y^{(\xi)2}m_z^{(\xi)2}\right) \qquad (\xi=1,2) \qquad (13a)$$

$$K_{MS} = -\frac{9}{4}\left[\lambda_{100}^2\left(c_{11}-c_{12}\right) - 2c_{44}\lambda_{111}^2\right] \qquad (13b)$$

goes as $W_{MS} \sim O(m^4)$ while $W_{MEL} \sim O(m^2)$, so that magnetostriction generally yields only a minor correction to the overall Hamiltonian [27]. For consistency, in the following, we shall neglect also the cubic terms appearing in the expression of magnetocrystalline anisotropy field (4c), since they are of the same order of magnitude as the magnetostriction terms. In fact, it is known that in cubic materials the energies of the magnetostriction and cubic anisotropy share the same functional dependence (the constant K_{MS} may be, indeed, incorporated into K_C). Therefore, in (4c) we will retain only the linear terms.

From now on, for simplicity, we shall assume that the electric field **E** has only one non-zero component with modulus E. This assumption, simply, means that there exists only one pair of lateral electrodes through which the bias voltage V is applied to the PZ layer (as it is schematically shown in Fig.1).

Considering all the above formulated definitions and assumptions, we can define the effective fields (2) as:

$$\gamma \mathbf{h}_{EFF}^{(1)} = -\frac{\omega_{exc}}{2}\mathbf{m}^{(2)} - \omega_H m_z^{(1)}\mathbf{e_z} + \omega_E m_y^{(1)}\mathbf{e_y} - \omega_C\left(m_x^{(1)}\mathbf{e_x} + m_y^{(1)}\mathbf{e_y} + m_z^{(1)}\mathbf{e_z}\right) +$$
$$-\omega_{M1}\left(\varepsilon_{xx}m_x^{(1)}\mathbf{e_x} + \varepsilon_{yy}m_y^{(1)}\mathbf{e_y} + \varepsilon_{zz}m_z^{(1)}\mathbf{e_z}\right) - \omega_{M2}\varepsilon_{yz}\left(m_y^{(1)}\mathbf{e_y} + m_z^{(1)}\mathbf{e_z}\right) \qquad (14a)$$

$$\gamma \mathbf{h}_{EFF}^{(2)} = -\frac{\omega_{exc}}{2}\mathbf{m}^{(1)} - \omega_H m_z^{(2)}\mathbf{e_z} + \omega_E m_y^{(2)}\mathbf{e_y} - \omega_C\left(m_x^{(2)}\mathbf{e_x} + m_y^{(2)}\mathbf{e_y} + m_z^{(2)}\mathbf{e_z}\right) +$$
$$-\omega_{M1}\left(\varepsilon_{xx}m_x^{(2)}\mathbf{e_x} + \varepsilon_{yy}m_y^{(2)}\mathbf{e_y} + \varepsilon_{zz}m_z^{(2)}\mathbf{e_z}\right) - \omega_{M2}\varepsilon_{yz}\left(m_y^{(2)}\mathbf{e_y} + m_z^{(2)}\mathbf{e_z}\right) \qquad , \qquad (14b)$$

where

$$\omega_{exc} = \gamma H_{exc}/M_S, \quad \omega_H = 2\gamma K_H/\left(\mu_0 M_S^2\right), \quad \omega_E = 2\gamma K_E/\left(\mu_0 M_S^2\right), \quad \omega_C = 2\gamma K_C/\left(\mu_0 M_S^2\right) \qquad (14c)$$

$$\omega_{M1} = 2\gamma B_1/\left(\mu_0 M_S^2\right), \quad \omega_{M2} = 2\gamma B_2/\left(\mu_0 M_S^2\right).$$

Notice, that in contrast with [9], where the cubic anisotropy was ignored, in our current calculation the *cubic* crystal symmetry is responsible for the appearance of an additional anisotropy term with the coefficient ω_C, and two magnetoelastic terms with the coefficients ω_{M1} and ω_{M2} arising due to the principal and shear strains, respectively.

We can now rewrite the LLGS equations for sublattice magnetizations in terms of the Neel vector $\mathbf{l} = \left(\mathbf{m}^{(1)} - \mathbf{m}^{(2)}\right)/2$, describing the antiferromagnetic order parameter, and of the slave variable $\mathbf{m} = \left(\mathbf{m}^{(1)} + \mathbf{m}^{(2)}\right)/2$ [4, 11, 28]. Manipulating (1), (14a), (14b), under the assumptions $|\mathbf{l}|^2 = 1$ and

$|\mathbf{m}| \Box |\mathbf{l}|$ (the latter one is valid when the exchange field is much larger than any other magnetic field in the AFM), we get:

$$\mathbf{m} \Box \frac{\dot{\mathbf{l}} \times \mathbf{l}}{\omega_{exc}} \ , \tag{15}$$

which allows us to derive the so-called "*sigma model*" equation for the Neel vector [11] :

$$\mathbf{l} \times \left(\frac{1}{\omega_{exc}} \ddot{\mathbf{l}} + \alpha_G \dot{\mathbf{l}} + \boldsymbol{\Omega} \cdot \mathbf{l} + \tau (\mathbf{l} \times \mathbf{p}) \right) = \mathbf{0} \tag{16}$$

where, according to (12), the AFM anisotropy matrix $\boldsymbol{\Omega}$, in frequency units, can be expressed as:

$$\boldsymbol{\Omega}(\mathbf{E}) = \begin{bmatrix} -\eta \omega_{M1} \left(\varepsilon_{yy}(\mathbf{E}) + \varepsilon_{zz}(\mathbf{E}) \right) + \omega_C & 0 & 0 \\ 0 & \omega_{M1} \varepsilon_{yy}(\mathbf{E}) - \omega_E + \omega_C & \omega_{M2} \varepsilon_{yz}(\mathbf{E}) \\ 0 & \omega_{M2} \varepsilon_{yz}(\mathbf{E}) & \omega_{M1} \varepsilon_{zz}(\mathbf{E}) + \omega_H + \omega_C \end{bmatrix} \tag{17}$$

In the anisotropy matrix (17), we have highlighted the dependence of the magnetoelastic terms on the electric field $\mathbf{E}$ generated through the PZ layer. Equation (17) also shows that the presence of the shear strains terms ε_{yz} makes the anisotropy matrix non-diagonal.

Let us now investigate the magnetic ground state of the AFM layer admitted by the model (16), (17), and address the small-amplitude dynamics of the AFM magnetization around such a ground state.

To this aim, let us consider the Neel vector as a sum of a static part $\mathbf{l_0}$, describing the ground state, and a dynamic part, describing the auto-oscillation $\mathbf{s}$ with the frequency ω.

$$\mathbf{l} = \mathbf{l_0} + \mathbf{s}e^{-i\omega t} \tag{18}$$

that satisfy the orthogonality constraint $\mathbf{l_0} \cdot \mathbf{s} = 0$. In the following subsections, we will treat the static and dynamic solutions separately.

2.1 Static solution of the AFM "sigma model" equation

The static solution of (16), using (17), (18), is given by:

$$\mathbf{l_0} \times \left(\boldsymbol{\Omega} \cdot \mathbf{l_0} + \tau (\mathbf{l_0} \times \mathbf{p}) \right) = \mathbf{0} . \tag{19}$$

Assuming that the spin-polarization vector $\mathbf{p}$ is directed along $\mathbf{e_z}$, and applying the vector product by $\mathbf{l_0}$ from the left to equation (19), we obtain:

$$\mathbf{l_0} \times \mathbf{l_0} \times \boldsymbol{\Omega} \cdot \mathbf{l_0} + \tau \mathbf{l_0} \times \left((\mathbf{l_0} \cdot \mathbf{e_z}) \mathbf{l_0} - \mathbf{e_z} \right) = \mathbf{0} \tag{20}$$

and, after simplification, we get:

$$(\mathbf{\Omega} - h\mathbf{I}) \cdot \mathbf{l_0} = \tau (\mathbf{e}_z \times \mathbf{l_0}) \tag{21}$$

where $h = \mathbf{l_0} \cdot (\mathbf{\Omega} \cdot \mathbf{l_0})$ is the effective staggered field and $\mathbf{I}$ is the identity matrix.

Let us express the ground state $\mathbf{l_0}$ using spherical coordinates as:

$$\mathbf{l_0} = (\sin\phi\sin\theta, \cos\phi\sin\theta, \cos\theta), \tag{22}$$

and reformulate the effective staggered field in the ϕ, θ-coordinates as:

$$h = \left(\tilde{A}\sin^2\phi + \tilde{B}\cos^2\phi\right)\sin^2\theta + \tilde{C}\cos\phi\sin 2\theta + \tilde{D}\cos^2\theta \tag{23}$$

where:

$$
\begin{aligned}
\tilde{A} &= -\eta\omega_{M1}\left(\varepsilon_{yy}(\mathbf{E}) + \varepsilon_{zz}(\mathbf{E})\right) + \omega_C \\
\tilde{B} &= \omega_{M1}\varepsilon_{yy}(\mathbf{E}) - \omega_E + \omega_C \\
\tilde{C} &= \omega_{M2}\varepsilon_{yz}(\mathbf{E}) \\
\tilde{D} &= \omega_{M1}\varepsilon_{zz}(\mathbf{E}) + \omega_H + \omega_C
\end{aligned}
\tag{24}
$$

The vector quantity (21) in this case admits the following form of the mutually coupled equations:

$$
\begin{cases}
\left[\left(\tilde{A} - h\right)\sin\phi + \tau\cos\phi\right]\sin\theta = 0 \\
\left[\left(\tilde{B} - h\right)\cos\phi - \tau\sin\phi\right]\sin\theta + \tilde{C}\cos\theta = 0 \\
\tilde{C}\cos\phi\sin\theta + \left(\tilde{D} - h\right)\cos\theta = 0
\end{cases}
\tag{25}
$$

When the dielectric polarization and electric field are parallel to each other $\mathbf{\Pi} \| \mathbf{E}$, the shear strains will vanish $\varepsilon_{yz} = 0$, and all the above defined quantities can be determined explicitly. In this case, the parameter $\tilde{C} = 0$, so that expression (23) and the solution of (25) are given by:

$$
\begin{cases}
\theta = \pi/2 \\
\phi = \dfrac{1}{2}\arcsin\dfrac{2\tau}{\omega_{M1}\left(\eta\varepsilon_{zz}(\mathbf{E}) + (1+\eta)\varepsilon_{yy}(\mathbf{E})\right) - \omega_E} \\
h = \omega_C + \left[\omega_{M1}\varepsilon_{yy}(\mathbf{E}) - \omega_E\right]\cos^2\phi - \eta\omega_{M1}\left[\varepsilon_{yy}(\mathbf{E}) + \varepsilon_{zz}(\mathbf{E})\right]\sin^2\phi
\end{cases}
\tag{26}
$$

confirming that the absence of shear strains favors the ground state to lie in the xy plane.

Moreover, we can make the dependence on the electric field even more explicit by assuming that the electric field $\mathbf{E}$ has only one non-zero component, and that the PZ polarization $\mathbf{\Pi}$ and the electric field $\mathbf{E}$ are collinear. Under these assumptions, and using (12a), (12b), (12c) we get the following expression for azimuthal angle of the Neel vector:

$$\phi = \frac{1}{2}\arcsin\frac{-2\tau}{\omega_E\left(1-\beta E\right)} \tag{27}$$

where the parameter $\beta = \omega_{M1}\left(\varepsilon_{yy} - \varepsilon_{xx}\right)/\omega_E$ measures the strain-induced anisotropy dependence on the electric field [9], while the quantity

$$\omega_{eff} = \omega_E\left(1-\beta E\right) \tag{27a}$$

represents the characteristic frequency of the effective easy-plane anisotropy that is modulated by the electric field applied to the PZ layer through the magnetoelastic effect. In the Table I we present the expressions for the staggered field h and the parameter β, as functions of the relative orientations of the poling vector $\mathbf{\Pi}$ and the electric field $\mathbf{E}$.

From Eq. (27) we can explicitly determine the "ignition" threshold current density J_{th}, corresponding to the excitation of the dynamical THz-frequency oscillations in the AFM:

$$J_{th} = \frac{\omega_E\left(1-\beta E\right)}{2\sigma} \tag{28}$$

which formally coincides with the threshold current found in [9].

It is interesting to note that, independently of the existence of the shear strains, the staggered field h is affected by the easy-plane (ω_E) and cubic (ω_C) anisotropies and, also, by the mechanical strains induced by the electric field $\mathbf{E}$ applied to the PZ layer [9].

Poling and Electric field direction	Staggered field	Parameter β
$\mathbf{\Pi}\parallel\mathbf{E}\parallel\mathbf{e_x}$	$h = \omega_C + \left[\omega_{M1}d_2E - \omega_E\right]\cos^2\phi - 2\eta\omega_{M1}d_2E\sin^2\phi$	$\dfrac{\omega_{M1}\left(1+2\eta\right)d_2}{\omega_E}$
$\mathbf{\Pi}\parallel\mathbf{E}\parallel\mathbf{e_y}$	$h = \omega_C + \left[\omega_{M1}d_1E - \omega_E\right]\cos^2\phi - \eta\omega_{M1}\left(d_1+d_2\right)E\sin^2\phi$	$\dfrac{\omega_{M1}\left[\left(1+\eta\right)d_1 + \eta d_2\right]}{\omega_E}$
$\mathbf{\Pi}\parallel\mathbf{E}\parallel\mathbf{e_z}$	$h = \omega_C + \left[\omega_{M1}d_2E - \omega_E\right]\cos^2\phi - \eta\omega_{M1}\left(d_1+d_2\right)E\sin^2\phi$	$\dfrac{\omega_{M1}\left[\eta d_1 + \left(1+\eta\right)d_2\right]}{\omega_E}$

Table I. Staggered field h and parameter β as functions of the common direction of the electric field and the dielectric polarization in the case when the shear strains are absent.

2.2 Dynamic solution of the AFM "sigma model" equation

Taking into account Eqs. (17) and (18), Eq.(16) can be represented as:

$$\left(\frac{\omega^2}{\omega_{exc}}+h\right)\mathbf{s}+\mathbf{l_0}\times(\mathbf{l_0}\times\mathbf{\Omega s})+\tau(\mathbf{l_0}\cdot\mathbf{e_z})(\mathbf{l_0}\times\mathbf{s})=0\,,\tag{29}$$

which can be rewritten as a homogeneous linear system **Ys=0** with the matrix **Y** having the form:

$$\mathbf{Y}=\begin{bmatrix}\dfrac{\omega^2}{\omega_{exc}}+h+\tilde{A}\left(l_{0_x}^2-1\right) & l_{0_x}\left(\tilde{B}l_{0_y}+\tilde{C}l_{0_z}\right)-\tau l_{0_z}^2 & l_{0_x}\left(\tilde{C}l_{0_y}+\tilde{D}l_{0_z}\right)+\tau l_{0_y}l_{0_z} \\[2mm] \tilde{A}l_{0_x}l_{0_y}+\tau l_{0_z}^2 & \dfrac{\omega^2}{\omega_{exc}}+h+\tilde{B}\left(l_{0_y}^2-1\right)+\tilde{C}l_{0_y}l_{0_z} & \tilde{D}l_{0_y}l_{0_z}+\tilde{C}\left(l_{0_y}^2-1\right)-\tau l_{0_x}l_{0_z} \\[2mm] \tilde{A}l_{0_x}l_{0_z}-\tau l_{0_y}l_{0_z} & \tilde{B}l_{0_y}l_{0_z}+\tilde{C}\left(l_{0_z}^2-1\right)+\tau l_{0_x}l_{0_z} & \dfrac{\omega^2}{\omega_{exc}}+h+\tilde{D}\left(l_{0_z}^2-1\right)+\tilde{C}l_{0_y}l_{0_z}\end{bmatrix},\tag{30}$$

where the components of the static vector $\mathbf{l_0}=\left(l_{0_x},l_{0_y},l_{0_z}\right)$ are given in (22).

Let us, first, investigate the solutions of the equation **Ys=0** in the presence of shear strains ($\tilde{C}\neq0$). By imposing the condition det**Y**=0, we end up with the following *bicubic* equation for the eigenfrequency ω:

$$\frac{\omega^6}{\omega_{exc}^3}+\kappa_4\frac{\omega^4}{\omega_{exc}^2}+\kappa_2\frac{\omega^2}{\omega_{exc}}+\kappa_0=0\,,\tag{31a}$$

where

$$\kappa_4=3h+\tilde{A}\left(l_{0_x}^2-1\right)+\tilde{B}\left(l_{0_y}^2-1\right)+\tilde{D}\left(l_{0_z}^2-1\right)+2\tilde{C}l_{0_y}l_{0_z}\tag{31b}$$

$$\kappa_2=3h^2+\left[2\tilde{A}\left(l_{0_x}^2-1\right)+2\tilde{B}\left(l_{0_y}^2-1\right)+2\tilde{D}\left(l_{0_z}^2-1\right)+4\tilde{C}l_{0_y}l_{0_z}\right]h+$$
$$+\left(\tilde{B}\tilde{D}-\tilde{C}^2\right)l_{0_x}^2+\tilde{A}\left(\tilde{B}l_{0_z}^2+\tilde{D}l_{0_y}^2-2\tilde{C}l_{0_y}l_{0_z}\right)+\tau^2l_{0_z}^2\tag{31c}$$

$$\kappa_0=\left[\tilde{A}l_{0_x}^2+\tilde{B}l_{0_y}^2+\tilde{D}l_{0_z}^2+2\tilde{C}l_{0_y}l_{0_z}\right]h^2+\tilde{A}\left(\tilde{B}\tilde{D}-\tilde{C}^2\right)+\tau^2\tilde{D}+$$
$$+\left[\left(\tilde{B}\tilde{D}-\tilde{C}^2\right)\left(l_{0_x}^2-1\right)+\tilde{A}\tilde{D}\left(l_{0_y}^2-1\right)+\left(\tilde{A}\tilde{B}+\tau^2\right)\left(l_{0_z}^2-1\right)-2\tilde{A}\tilde{C}l_{0_y}l_{0_z}\right]h\tag{31d}$$

The explicit analytical solution of (31a) is rather cumbersome, so the information about the frequency of the excited eigenmode will be obtained numerically in the following section of the paper. However, it is known that, in the passive subcritical regime, the sigma model admits two real and positive roots only. This clearly suggests that the third root of (31a), being real and negative, is unphysical and has to be ignored.

Om the other hand, if the dielectric polarization vector $\mathbf{\Pi}$ and the electric field $\mathbf{E}$ are parallel to each other, no shear strains are generated ($\tilde{\mathcal{C}} = 0$), and the ground state $\mathbf{l_0}$ lies in the xy plane and is orthogonal to the spin-polarization $\mathbf{p} \equiv \mathbf{e_z}$. In such a case, the dynamic equation (29) can be simplified to:

$$\left(\mathbf{P_{l_0}} \left(\mathbf{\Omega} - h\mathbf{I} \right) - \frac{\omega^2}{\omega_{exc}} \mathbf{I} \right) \mathbf{s} = \mathbf{0}, \tag{32}$$

where $\mathbf{P_{l_0}} = \mathbf{I} - \mathbf{l_0} \otimes \mathbf{l_0}$. In such a configuration it is possible to obtain the expressions of the two AFM eigenmode frequencies explicitly. The frequency of the lowest AFM eigenmode is formally given by:

$$\omega_1 = \sqrt{\omega_{exc} \left[\omega_E \left(1 - \beta E \right) \right] \cos 2\phi}, \tag{33}$$

where the coefficient β varies with the variation of the polarization vector $\mathbf{\Pi}$ and the electric field $\mathbf{E}$ directions as it is presented in Table I. The expressions for the frequency ω_2 of the high-frequency AFM eigenmode are presented in Table II.

We can conclude that, in the absence of shear strains, the expression for the frequency of the lowest AFM eigenmode is formally the same as the one found in the case when the cubic anisotropy is neglected. So, the frequency of the lowest AFM eigenmode is unaffected by the cubic anisotropy (the azimuthal angle ϕ, appearing in (33) and in Table II, is independent of ω_C).

In contrast, the expression for the frequency of the high-frequency AFM eigenmode varies with the variation of the poling and electric field directions, and, in the presence of shear strains, the cubic anisotropy brings a non-zero contribution to the frequency of the higher frequency AFM eigenmode (the frequency of the higher eigenmode obtained from the solution of (31a), indeed, depends on h, θ and ϕ, which, in turn, vary with the variation of ω_C according to Eq. (25)).

Poling and Electric field direction	High-frequency mode
$\mathbf{\Pi} \parallel \mathbf{E} \parallel \mathbf{e_x}$	$\omega_2 = \sqrt{\omega_{exc} \left[\omega_H + \omega_{M1} d_2 E + \left(\omega_E - \omega_{M1} d_2 E \right) \cos^2 \phi + 2\eta \omega_{M1} d_2 E \sin^2 \phi \right]}$
$\mathbf{\Pi} \parallel \mathbf{E} \parallel \mathbf{e_y}$	$\omega_2 = \sqrt{\omega_{exc} \left[\omega_H + \omega_{M1} d_2 E + \left(\omega_E - \omega_{M1} d_1 E \right) \cos^2 \phi + \eta \omega_{M1} \left(d_1 + d_2 \right) E \sin^2 \phi \right]}$
$\mathbf{\Pi} \parallel \mathbf{E} \parallel \mathbf{e_z}$	$\omega_2 = \sqrt{\omega_{exc} \left[\omega_H + \omega_{M1} d_1 E + \left(\omega_E - \omega_{M1} d_2 E \right) \cos^2 \phi + \eta \omega_{M1} \left(d_1 + d_2 \right) E \sin^2 \phi \right]}$

Table II. The frequency of the higher AFM eigenmode as a function of the poling and electric field directions, in the absence of shear strains.

3. Numerical results

The analysis carried out so far has revealed that the anisotropy matrix $\mathbf{\Omega}$ given by Eq. (17) is affected by the magnetoelastic contribution arising from the coupling between the PZ layer and the AFM layer [9]. Variation of the AFM anisotropy, due to the application of the bias electric field $\mathbf{E}$, affects the AFM ground state (h, θ, ϕ), the ignition threshold current J_{th}, and both eigenmode frequencies ω_1 and ω_2 (albeit to a different extent).

The goal of this section is to evaluate numerically the influence of the applied electric field on the physical quantities studied analytically in the previous section, and to find the optimum setup which guarantees the maximum control of the AFM anisotropy by the applied electric field. To determine the "optimum setup", our analysis assumes that two key degrees of freedom will be used for the AFM anisotropy control: the choice of the ceramic PZ material (which affects the coefficients d_1, d_2 and d_4) and the relative orientation of the dielectric polarization vector $\mathbf{\Pi}$ and the applied electric field $\mathbf{E}$ (which affects the structure of the strain tensor ε_{ij} and, consequently, modifies the analytical expression for the involved physical quantities). In carrying out this investigation, we also evaluate how the *cubic* anisotropy of the AFM material influences the results, in comparison with the case when this anisotropy was ignored.

For simplicity, in Tables III we presented the numerical values of parameters applicable to the case when the AFM layer is made of a monocrystalline NiO and in Table IV those of derived parameters. To perform a quantitative comparative analysis, we took into account the most common ceramic PZ materials, PZT4, PZT5A, PZT5H, PZT6B, PZT7A, PZT8 and BaTiO$_3$, and for each of them computed the dielectric coefficients d_1, d_2 and d_4 (see Table V). Let us now analyse the obtained results paying attention to the relative orientation of the dielectric polarization and the electric field.

3.1   Dielectric polarization parallel to the electric field ($\mathbf{\Pi} \parallel \mathbf{E}$)

Let us, first, consider the case when the dielectric polarization $\mathbf{\Pi}$ and the applied electric field $\mathbf{E}$ are parallel to each other, and are directed along one of the reference axes. In this configuration, no shear strains act on the AFM layer. We can, then, evaluate numerically the parameter β that measures the strain-induced anisotropy dependence on the modulus of the electric field E that needs to be optimized [9]. The results presented in the Table V show that, independently of the poling direction, the PZ material exhibiting the largest (absolute) value of β is PZT5H. The results also indicate that, in the best setup, the PZ layer should be polarized along the y axis (i.e. along the easy axis of the AFM layer) with lateral electrodes

placed on the *xz* faces, in order to generate the electric field parallel to the vector of dielectric polarization **Π**.

According to our estimation, such a setup would allow one to achieve the largest β value $\beta=18.18\times10^{-7}$ m/V. For comparison, the results obtained in the previous work [9], based on the assumptions that the AFM material has no cubic anisotropy, the magnetoelastic energy takes the form associated to isotropic materials and that $\mathbf{\Pi} \parallel \mathbf{E} \parallel \mathbf{e_x}$, reported the β value of 1.64×10^{-7} m/V, i.e. more than one order of magnitude smaller.

In order to better appreciate the improvement achieved by varying the common orientation of the dielectric polarization and electric field, let us now evaluate numerically the most relevant quantities obtained in the previous section. In Fig.2 we demonstrate behaviour of the main characteristics of the auto-oscillations in a PZ/AFM/HM structure obtained by varying the common direction of the dielectric polarization **Π** and the electric field **E** along the reference axes. In particular, in Figs.2(a-c) we show the dependence of the effective easy-plane anisotropy frequency ω_{eff} (14c), the ignition threshold current J_{th} (28), and the lowest AFM eigenfrequency ω_1 (33) as a function of the modulus of the electric field E, whereas in Fig.2(d) we present ω_1 as a function of the subcritical current density J flowing in the HM layer. These results clearly demonstrate that it is possible to effectively control the main characteristics of the auto-oscillations of the AFM layer by varying the common direction of the dielectric polarization and the electric field relative to the reference axes of the layered PZ/AFM/HM structure.

Let us discuss in more detail the results related to the optimum setup, $\mathbf{\Pi} \parallel \mathbf{E} \parallel \mathbf{e_y}$ (red curves in Fig.2), which also corresponds to the only orientation of the electric field **E** giving a positive coefficient β (see Table V). In such a case, the effective frequency ω_{eff} is decreased by more than 3 GHz when the electric field is swept from -5 to $+5\times10^5$ V/m (Fig.2a).

Note that variation of the electric field from -5 to $+5\times10^5$ V/m can lead to a substantial reduction of ignition threshold current for the excitation of auto-oscillations in the AFM layer, which completely vanishes at $E=1/\beta\approx5.5\times10^5$ V/m (see Fig.2b). This reduction of the threshold current induced by the electric field applied to the PZ layer could be of a critical importance for the practical realization of the sub-THz frequency excitations in the PZ/AFM/HM layered structures.

In the absence of the electric current in the HM layer, the same range of the electric field variation leads to the tuning of the frequency of the lowest AFM eigenmode (i.e. the lowest frequency of the antiferromagnetic resonance (AFMR)) from 0.3 THz to 0 (see dashed red line in Fig.2c). When an electric current of $J=J_0=2\times10^{12}$ A/m^2 is injected into the HM layer, the same tuning range of the lowest AFMR frequency can be achieved in a twice smaller range of variation of the bias electric field (see solid red line

in Fig.2c). In general, Fig. 2d demonstrates that combination of the current and electric field controls allowed one to tune the AFMR frequency of the AFM layer in a wide range in a subcritical regime (no generation of auto-oscillations) when the PZ/AFM/HM layered structure can be used as a tunable resonance receiver of the sub-THz electromagnetic signals [8].

Parameter	Value	References
M_S	351 kA/m	[29]
α_G	3.5×10^{-3}	[29, 30, 31]
H_{exc}	780×10^6 A/m	[29, 32]
K_H	280 kJ/m^3	[33]
K_E	10.9 kJ/m^3	[33]
K_C	30.0 kJ/m^3	[34, 35]
c_{11}	225 GPa	[36, 37]
c_{12}	95 GPa	[36, 37]
c_{44}	110 GPa	[36, 37]
λ_{100}	-140×10^{-6}	[38, 39]
λ_{111}	-79×10^{-6}	[38, 39]

Table III. Main parameters of AFM layer (monocrystalline NiO).

Derived Parameters	Value
σ	$2\pi \times 4.32 \times 10^{-4}$ Hz m^2/A Hz·m^2/A
η	0.42
B_1	27.30×10^6 J/m^3
B_2	26.07×10^6 J/m^3
ω_{exc}	$2\pi \times 27.45$ THz
ω_H	$2\pi \times 44.69$ GHz
ω_E	$2\pi \times 1.74$ GHz
ω_C	$2\pi \times 4.79$ GHz
ω_{M1}	$2\pi \times 4.36$ THz
ω_{M2}	$2\pi \times 4.16$ THz

Table IV. Derived parameters for the PZ/AFM/HM layered structure.

Material	d_1 (×10^{-10})	d_2 (×10^{-10})	d_4 (×10^{-10})	$\beta\,(\Pi\|\mathbf{E}\|\mathbf{e_x})$ (×10^{-7})	$\beta\,(\Pi\|\mathbf{E}\|\mathbf{e_y})$ (×10^{-7})	$\beta\,(\Pi\|\mathbf{E}\|\mathbf{e_z})$ (×10^{-7})
PZT4	+2.89	−1.23	+4.96	−5.67	+9.00	−1.31
PZT5A	+3.74	−1.71	+5.83	−7.89	+11.53	−2.12
PZT5H	+5.92	−2.74	+7.39	−12.65	**+18.18**	−3.49
PZT6B	+0.72	−0.27	+1.29	−1.27	+2.27	−0.22
PZT7A	+1.53	−0.65	+3.64	−3.00	+4.77	−0.69
PZT8	+2.15	−0.93	+3.32	−4.31	+6.67	−1.05
BaTiO$_3$	+1.91	−0.79	+2.59	−3.64	+5.98	−0.78

Table V. Dielectric coefficients for the most commonly used ceramic PZ materials (taken from [26]), and the corresponding values of the coefficient β (taken from Table I) as functions of the common direction of the dielectric poling Π and electric field $\mathbf{E}$. All the quantities are expressed in m/V. The marked cell represents the best result.
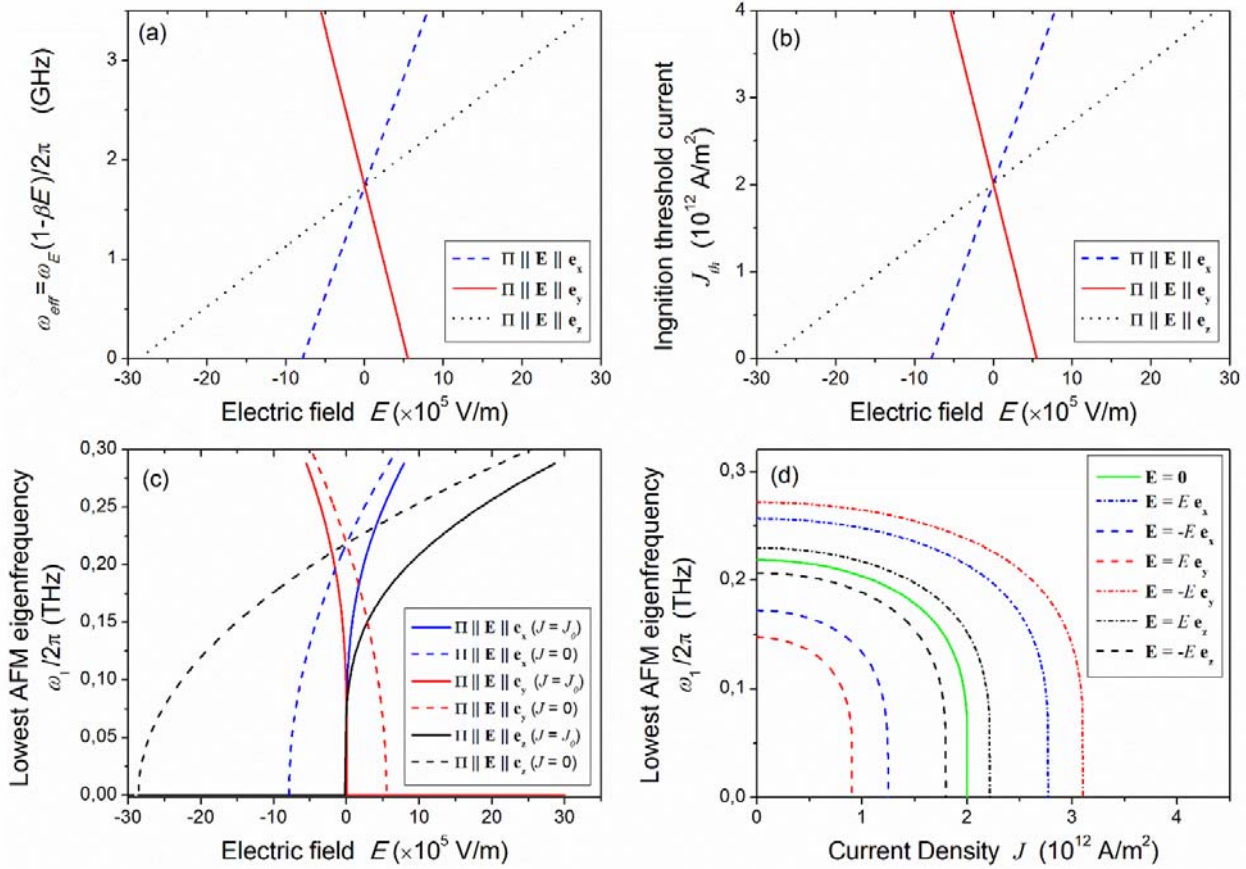
Fig.2. Main characteristics of the auto-oscillations in a PZ/AFM/HM structure obtained by varying the common direction of the dielectric polarization Π and the electric field $\mathbf{E}$ along the reference axes: (a) Effective frequency ω_{eff} (see (14c)) ; (b) Ignition threshold current J_{th} (see (28)) in the HM layer corresponding to the excitation of the lowest AFM eigenmode; (c) Frequency of the lowest AFM eigenmode ω_1 (see (33)) as functions of the modulus of the electric field E. In (c) the frequency is shown for two different values of the current density in the HM layer: $J=0$ A/m^2 (dashed lines) and $J=J_0=2\times10^{12}$ A/m^2 (solid lines); (d) Frequency of the lowest AFM eigenmode ω_1 as a function of the subcritical current density J, for zero electric field $E=0$ (solid green curve) and $E=3\times10^5$ V/m directed along one of the reference axes (non-solid curves). In all the figures, the blue, red and black curves correspond to the cased when the electric field is $\mathbf{E}$ directed along the axes x, y and z, respectively.

3.2   Dielectric polarization orthogonal to the electric field (Π ⊥ E)

In this section, we summarize the results obtained when the dielectric polarization **Π** is orthogonal to the electric field **E**, in particular for $\mathbf{\Pi} \equiv \mathbf{e_y}$ and $\mathbf{E} \Box \mathbf{e_z}$ or $\mathbf{\Pi} \equiv \mathbf{e_z}$ and $\mathbf{E} \Box \mathbf{e_y}$. As it was explained above, in such a configuration the AFM layer is subject to non-zero shear strains.

First of all, we need to establish which PZ material provides the best tunability of the AFMR frequency by electric field. To this aim, in Fig.3(a-d) we present the frequency ω_1 of the lowest AFM eigenmode (lowest AFMR frequency) as a function of the electric field E, obtained by solving numerically Eqs. (25) and (31) for different ceramic PZ materials and for different values of the bias electric current J ((a) J=0 A/m^2, (b) J=2×10^{12} A/m^2, (c) J=2.25×10^{12} A/m^2, (d) J=2.5×10^{12} A/m^2).
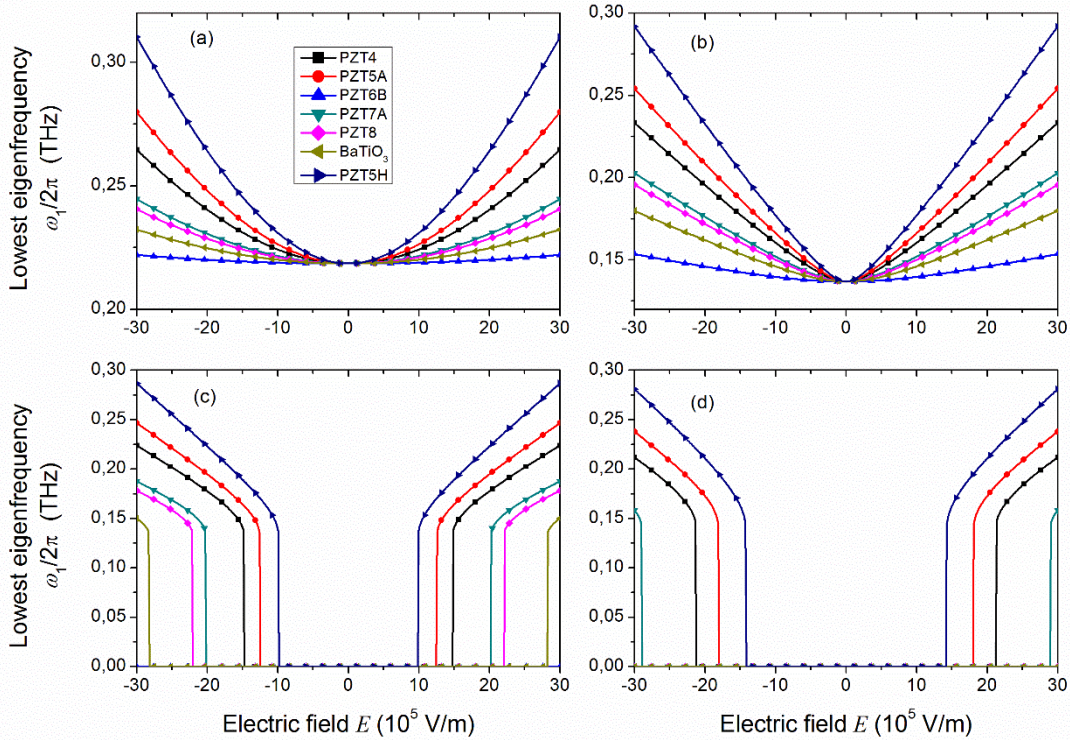
Fig.3. Frequency of the lowest AFM eigenmode (lowest AFMR frequency) as a function of the electric field applied to the PZ layer in the case of dielectric polarization **Π** orthogonal to the electric field **E**. The different curves correspond to the response of different ceramics PZ materials (as shown in the inset in Fig.3a). The four panels a-d demonstrate the lowest eigenmode frequency for different (subcritical) electric currents injected in the HM layer: (a) J=0 A/m^2, (b) J=2×10^{12} A/m^2, (c) J=2.25×10^{12} A/m^2, (d) J=2.5×10^{12} A/m^2.

The analysis of data presented in Fig.3 allows us to make the following conclusions. First, the PZ material that exhibits the best frequency tuning turns out to be, again, the PZT5H. Indeed, independently of the value of the injected electric current J, this material allows one to achieve the largest frequency tuning

for a fixed value of electric field E or, equivalently, it requires the smallest variation of the electric field magnitude to achieve a given change of the AFMR frequency.

Numerical results presented in Fig.3 also reveal that, in contrast to the case $\mathbf{\Pi} \parallel \mathbf{E}$, the AFMR frequency obtained in the presence of only the *shear* strains *increases* with the increase of the electric field magnitude, and this dependence is symmetric, and does not change when the electric field (and, therefore, the voltage V) changes its sign from positive to negative. It is also clear from Fig.3, that the lowest AFMR frequency ω_1 changes its functional dependence on the modulus of the electric field E when the magnitude of the injected current J is varied. Indeed, ω_1 is an increasing function of E, and it is quadratic for $J=0$ (Fig.3a), almost linear for $J=2\times10^{12}$ A/m^2 (Fig.3b), and becomes similar to a square root for larger current densities (Figs.3c,d). This feature of the frequency dependence on the electric field makes it impossible to determine the "equivalent-β" coefficient for the configuration $\mathbf{\Pi} \perp \mathbf{E}$.

Moreover, the AFM effective anisotropy, and, therefore, the lowest AFMR frequency, rapidly decreases with current, and vanishes for sufficiently large driving currents. Thus, in the current-driven PZ/AFM/HM structure where the electric field is perpendicular to the dielectric polarization the AFMR frequency is non-zero only in a range of rather high magnitudes of the electric field E (see Fig.3 c,d).

The fact that the AFM effective anisotropy and, therefore, the lowest AFMR frequency, in the perpendicular configuration $\mathbf{\Pi} \perp \mathbf{E}$, increase with the increase of E, basically, means that the threshold current for the excitation of auto-oscillations in AFM will only increase with the increase of the electric field modulus, so this geometry can be used for the design of passive resonance detectors of sub-THz frequencies, but not the active generators in this frequency range.

Indeed, the dependence of the injection threshold current on the voltage-induced electric field E demonstrates the quadratic increase (Fig.4a), while the AFMR frequency in the subcritical regime ($J < J_{th}$) decreases with the increase of the driving current in the HM layer electric current (Fig.4b) similar to the case of parallel geometry $\mathbf{\Pi} \parallel \mathbf{E}$ (see Fig.2d and Fig. 4 in [9]). For simplicity, in Fig.4 we presented only the case of the PZ material exhibiting the best performances (PZT5H).
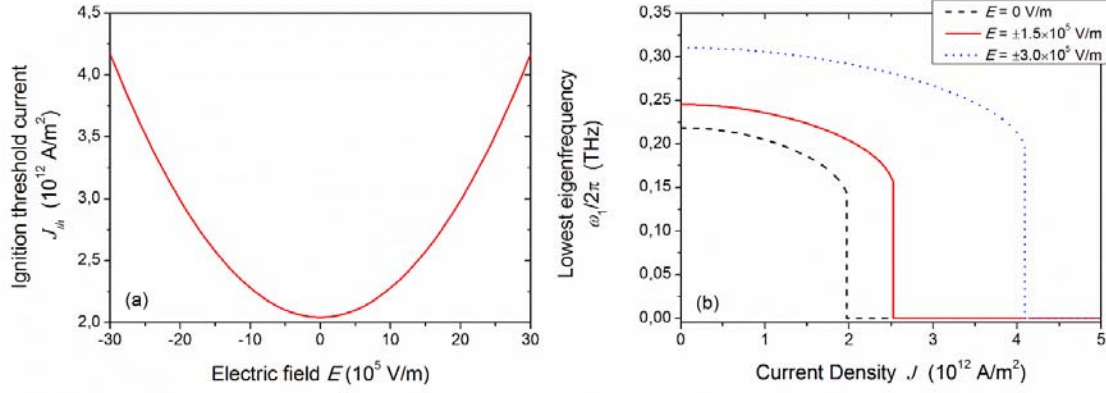
Fig.4. (a) Ignition threshold current as a function of electric field. (b) Lowest eigenfrequency as a function of current density J, for different values of the modulus of electric field E. Results correspond to the case of dielectric polarization Π of the PZT5H piezoelectric material orthogonal to the electric field $\mathbf{E}$.

4.   Conclusions

Our above presented theoretical results demonstrate that the AFMR frequency of the PZ/AFM/HM layered structure in a passive subcritical regime for both the parallel $\Pi \parallel \mathbf{E}$ and perpendicular $\Pi \perp \mathbf{E}$ geometries can be controlled by the external electric field applied to the PZ layer, and by the driving electric current flowing in the HM layer. In the parallel geometry for a proper direction of the applied electric field it is possible not only to reduce the AFMR frequency, but also to reduce the threshold needed for generation of auto-oscillations in the AFM layer (see Fig.2 b, c). Thus, the application of a properly directed electric field in parallel geometry may lead to the experimental observation of the auto-oscillation generation in PZ/AFM/HM layered structures at the experimentally reachable current densities in the HM layer, if the optimum combination of the PZ and AFM materials has been chosen (e.g. if PZT5H is used with NiO). If the electric field direction is reversed, both the generation threshold and the AFMR frequency are increased with the electric field magnitude, and the layered structure can be used as a passive electrically-tunable resonance detector of sub-THz electromagnetic signals. Our calculations in which the cubic anisotropy has been taken into account also demonstrated that the optimization of the material composition in the PZ/AFM/HM layered structure makes possible to achieve the increase in the electric field tenability coefficient β by more than one order of magnitude, compared to the previous calculation [9], where the influence of the AFM cubic anisotropy was ignored and the magnetoelastic contribution was ascribable to that of isotropic materials.

In the case of a perpendicular geometry $\Pi \perp \mathbf{E}$ both the ignition threshold and the AFMR frequency are increasing with the increase of the electric field modulus, and, therefore, the PZ/AFM/HM layered structure in this geometry can be used only as a passive tunable resonance detector.

Independently of the geometric configuration of Π and $\mathbf{E}$, the combination of the PZT5H PZ material with the NiO AFM material demonstrated the best tunability of the eigenmode properties of the studied layered structure using the variation of the electric field applied to the PZ ceramic layer. We firmly believe that the theoretical optimization and the following fabrication of PZ/AFM/HM layered structures, where AFM layer is both monocrystalline and mono-domain, will eventually lead to the development of practical current-driven THz-frequency oscillators [4] and tunable resonance detectors [8] controlled by an applied bias electric field.

REFERENCES

[1] V. Baltz, A. Manchon, M. Tsoi, T. Moriyama, T. Ono, and Y. Tserkovnyak, Rev. Mod. Phys. 90, 015005 (2018).

[2] T. Satoh, Y. Terui, R. Moriya, B.A. Ivanov, K. Ando, E. Saitoh, T. Shimura and K. Kuroda, Nat. Photon. 6, 662 (2012)

[3] X. Marti, et al., Nat. Mater. 13, 367 (2014).

[4] R. Khymyn, I. Lisenkov, V. Tiberkevich, B. A. Ivanov and A. Slavin, Sci. Rep. 7, 43705 (2017).

[5] O.R. Sulymenko, O.V. Prokopenko, V.S. Tiberkevich, A.N. Slavin, B.A. Ivanov, and R.S. Khymyn, Phys. Rev. Appl. 8, 064007 (2017).

[6] O. Gomonay, T. Jungwirth, and J. Sinova, Phys. Rev. B 98, 104430 (2018).

[7] R. Khymyn, V. Tiberkevich and A. Slavin, AIP Adv. 7, 055931 (2017).

[8] A. Safin, V. Puliafito, M. Carpentieri, G. Finocchio, S. Nikitov, P. Stremoukhov, A. Kirilyuk, V. Tyberkevych and A. Slavin, APL 117, 222411 (2020).

[9] P.A. Popov, A.R. Safin, A. Kirilyuk, S.A. Nikitov, I. Lisenkov, V. Tyberkevich and A. Slavin Phys. Rev. Appl. 13, 044080 (2020).

[10] B. A. Ivanov, Low Temp. Phys. 40, 91 (2014).

[11] E. G. Galkina and B. A. Ivanov, Low Temp. Phys. 44, 618 (2018)

[12] T. Chirac, J.-Y. Chauleau, P. Thibaudeau, O. Gomonay, and M. Viret, Phys. Rev. B 102, 134415 (2020).

[13] K. Fritsch, R. D'Ortenzio, and D. Venus, Phys. Rev. B 83, 075421 (2011).

[14] H. Kachkachi and D.S. Schmool, Eur. Phys. J. B 56, 27–33 (2007).

[15] Y.P. Kalmykov, S.V. Titov, W.T. Coffey, M. Zarifakis, and W. J. Dowling, Phys. Rev. B 99, 184414 (2019).

[16] W.T. Coffey, P.-M. Déjardin and Y.P. Kalmykov, Phys. Rev. B 79, 054401 (2009).

[17] M.V. Lopes, E.C. de Souza, J.G. Santos, J. Medeiros de Araujo, L. Lima, A. Barbosa de Oliveira, F. Bohn, and M. Assolin Correa, Sensors 20, 1387 (2020).

[18] G. Consolo, G. Valenti. J. Appl. Phys. 121, 043903 (2017).

[19] Y.C. Shu, M.P. Lin, K.C. Wu. Mech. Mater. 36, 975–997 (2004).

[20] L. Banas, Math. Methods Appl. Sci. 28, 1939–1954 (2005).

[21] C.Y. Liang, S.M. Keller, A.E. Sepulveda, A. Bur, W.-Y. Sun, K. Wetzlar, G. P. Carman, Nanotechnology 25, 435701 (2014).

[22] S. Federico, G. Consolo, G. Valenti. Math. Mech. Solids 24, 2814–2843 (2019).

[23] G. Consolo, S. Federico, G. Valenti, Ric. Matematica (2020), DOI:10.1007/s11587-020-00484-x.

[24] T. Nussle, P. Thibaudeau, S. Nicolis, J. Magn. Magn. Mater. 469, 633 (2019).

[25] G. Consolo, S. Federico, G. Valenti. Phys. Rev. B 101, 014405 (2020).

[26] J. Yang, An introduction to the theory of piezoelectricity. Springer (2006).

[27] M. Finazzi, P. Biagioni, A. Brambilla, L. Duò, and F. Ciccacci, Phys. Rev. B 72, 024410 (2005).

[28] H.V. Gomonay and V.M. Loktev. Phys. Rev. B 81, 144427 (2010).

[29] M.T. Hutchings and E.J. Samuelsen, Phys. Rev. B 6, 3447–3461 (1972).

[30] Y. Tserkovnyak, A. Brataas, G.E.W. Bauer and B.I. Halperin, Rev. Mod. Phys. 77, 1375–1421 (2005).

[31] H. Nakayama, K. Ando, K. Harii, T. Yoshino, R. Takahashi, Y. Kajiwara, K. Uchida, Y. Fujikawa and E. Saitoh, Phys. Rev. B 85, 144408 (2012).

[32] A.J. Sievers and M. Tinkham, Phys. Rev. 129, 1566–1571 (1963).

[33] C.R.H. Bahl, The magnetic properties of antiferromagnetic nanoparticles: NiO and Fe2O3, Risø National Laboratory. Risø PhD, No. 30(EN).

[34] K. Kurosawa, M. Miura and S. Saito, J. Phys. C: Solid State Phys. 13, 1521 (1980).

[35] A. Brambilla, Properties of NiO and Fe Magnetic Thin Films in Layered Structures, PhD thesis, Politecnico di Milano.

[36] A.G. Every, A.K. McCurdy, Second and Higher Order Elastic Constants, Springer (1992).

[37] P. du Plessis, S.J. van Tonder and L. Alberts, J. Phys. C 4, 1983 (1971).

[38] T.G. Phillips and R.G. White, Phys. Rev. 153, 616 (1967).

[39] I.P. Krug, Magnetic Proximity Effects in Highly-ordered Transition Metal Oxide Heterosystems studied by Soft X-Ray Photoemission Electron Microscopy, PhD thesis, The University of Duisburg-Essen (2008).